2024 IEEE International Conference on Robotics and Automation (ICRA 2024)
May 13-17, 2024. Yokohama, Japan

Boundary Factors for Seamless State Estimation between Autonomous Underwater Docking Phases

Aldo Terán Espinoza, Antonio Terán Espinoza, John Folkesson, Peter Sigray, Jakob Kuttenkeuler

***Abstract*— Autonomous underwater docking is of the utmost importance for expanding the capabilities of Autonomous Underwater Vehicles (AUVs). Due to a historical focus on underwater docking to only static targets, the research gap in underwater docking to dynamically active targets has been left relatively untouched. We address the state estimation problem that arises when trying to rendezvous a chaser AUV with a dynamic target by modeling the scenario as a factor graph optimization-based Simultaneous Localization and Mapping problem. We present a set of boundary factors that aid the inference process by seamlessly transitioning the target's state between the different observability stages, intrinsic to any dynamic docking scenario. We benchmark the performance of our approach using the Stonefish simulated environment.**

I. Introduction

Autonomous underwater docking is a key capability to enable a broad range of new missions for Autonomous Underwater Vehicles (AUVs): some examples include persistent underwater monitoring [1]–[3], underwater inspection and maintenance [4], [5], and unsupervised recovery and charging [6]–[9], among many others.

In our previous work [10], we borrowed concepts related to robotic spacecraft docking to label every instance of an underwater docking mission as a proximity operation (prox-op). Prox-ops consist of a chaser and a target agent that endure a set of different phases before reaching a rendezvous and continue with an arbitrary and target-specific joint operation [11]. We consider the most generic scenario to be that of a chaser seeking to rendezvous with a dynamically active target: in this scenario the chaser starts at a relatively large distance to its target and has to systematically solve a relative navigation problem up until the rendezvous.

Current works on underwater prox-ops focus mainly on docking to static targets, and thus never explicitly account for the representation changes with respect to the target that naturally occur as better sensing is enabled once the two agents get closer. Herein, we present optimization constraints in the form of factor graph boundary factors that allow us to model these changes of representations during an example docking scenario with a dynamic target. Furthermore, we use these factors to carry out seamless state estimation for both the chaser and an active target using the same estimator by posing the underlying estimation problem as a Simultaneous Localization and Mapping (SLAM) problem. Throughout this work, we derive the necessary measurement and motion models, and present simulation results from a dynamic underwater docking scenario.

This work was supported by the Stiftelsen för Strategisk Forskning (SSF) through the Swedish Maritime Robotics Centre (SMaRC)(IRC15-0046).

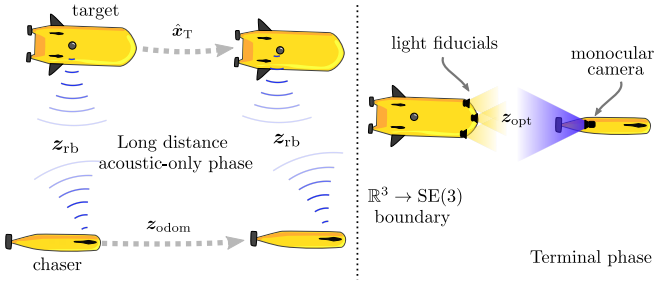

Fig. 1. Pictorial description of the underwater docking scenario tackled in this work. The scenario involves a chaser AUV and a dynamically active AUV as the target. During the long distance phase, only acoustic range-bearing relative measurements $\boldsymbol{z}_{\text{rb}}$ are available, constraining only the target's position in $\mathbb{R}^3$. Once the boundary to the terminal phase has been crossed, optical measurements $\boldsymbol{z}_{\text{opt}}$ are used to fully constrain the SE(3) pose of the target.

II. Related Work

The specific contribution we are addressing in the present work is the development of a state estimation solution to seamlessly transition between long- and short-range relative navigation scenarios for dealing with an active target. The need for an explicit state estimation pipeline, where the chaser explicitly reasons about the state of the target, is of the utmost importance for complex dynamic docking scenarios in order to inform the subsequent tasks and phases. This automatically renders most of the tracking-based docking methods found in the literature (e.g. [3], [12]–[14]) unrelated to our work. To further narrow our research gap, static docking solutions, even when including an explicit state estimation pipeline [15]–[18], also fall outside of our scope because they lack the problems intrinsic to the handling of a dynamic target. These conditions narrow down the contenders to only a few works that study dynamic scenarios: [7], [8], [19]–[21]. However, the works that do not fall into one of the aforementioned categories, either lack a thorough description of their methods [8], or do not specifically address the problems that arise during a full (long distance to terminal homing) docking scenario [19], [21]. In the following sections, we derive the required concepts and notions required to tackle the intricate problems that arise when estimating the state of a dynamic target during a full docking operation.

III. Problem Formulation

Underwater proximity operations are defined by a set of phases that the chaser agent has to navigate through in order to engage with its target. Two of the main phases, defined

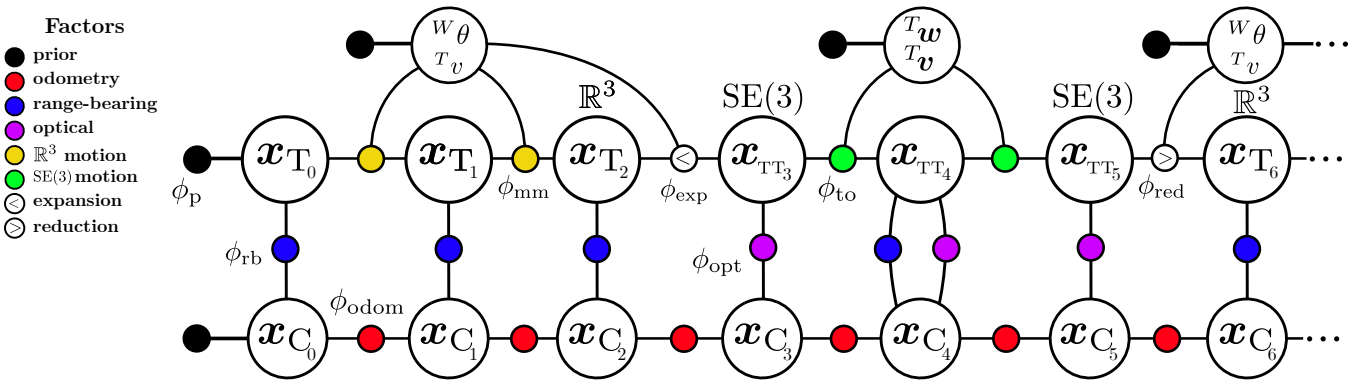

Fig. 2. Factor graph of the underlying estimation problem that arises from the underwater docking scenario depicted in Figure 1.

by the sensor availability for relative navigation, are: (i) the long distance phase, which is typically an acoustic navigation phase because of the unrivaled range capabilities of sound underwater, with the caveat that it only provides coarse information about the target; and (ii) the terminal phase, where newly enabled sensors provide much more granular information for the chaser to better resolve the target's state.

The example scenario at hand consists of a dynamic underwater docking operation, in which an AUV (the chaser) seeks to reach close proximity to another dynamically active AUV (the target), by passing through the two phases. During the long distance phase, the chaser uses only its on-board inertial navigation system (INS) and relative ultra-short baseline (USBL) acoustic measurements to estimate both its pose and the target's position (left side in Figure 1). During the terminal phase, the chasing AUV, equipped with a monocular camera, measures its relative pose to a set of light beacons (fiducials) mounted on the target AUV in a known pattern (right side in Figure 1). To provide the chaser with information regarding the dynamics of the target, simplifying assumptions on the motion of the target are used during the long distance phase, namely that the target will keep a constant (but unknown) velocity, heading, and depth [22].

The scenario we are addressing is that of finding the set of best chaser $\boldsymbol{x}_{\text{C}}$ and target states throughout the long distance $\boldsymbol{x}_{\text{T}}$ and terminal phase $\boldsymbol{x}_{\text{TT}}$ of the dynamic proximity operation described above. Figure 1 depicts the example scenario at hand. We define the state of the chaser $\boldsymbol{x}_{\text{C}}$ as the pose of the chaser expressed in the world frame W, i.e. ${}^{W}_{C}\mathbf{T} \in \text{SE}(3)$, where

$$ {}^{W}_{C}\mathbf{T} = \begin{bmatrix} {}^{W}_{C}\mathbf{R} & {}^{W}\boldsymbol{t}_{C/W} \\ \mathbf{0}^{\top} & 1 \end{bmatrix} $$

describes a rigid transformation in homogeneous coordinates. For clarity, we differentiate the target's state during the long distance phase $\boldsymbol{x}_{\text{T}} = {}^{W}\boldsymbol{t}_{T/W} \in \mathbb{R}^3$ which only contains the target's 3D position in the world frame W, and during the terminal phase, the state $\boldsymbol{x}_{\text{T}}$ is enhanced by adding the orientation component and representing it as a full 6-DoF pose $\boldsymbol{x}_{\text{TT}} = {}^{W}_{T}\mathbf{T} \in \text{SE}(3)$ in homogeneous coordinates.

The information used to estimate both agents' states consists of a set of measurements $\mathbf{Z}$ that include: (1) range and bearing measurements $\boldsymbol{z}_{\text{rb}}$ corresponding to the relative position ${}^{C}\boldsymbol{t}_{T/C}$ of the target T with respect to the chaser C, expressed in the chaser's body frame; (2) odometry measurements $\boldsymbol{z}_{\text{odom}} = {}^{C_i}_{C_{i+1}}\mathbf{T}$ which describe a change in the chaser's pose between discrete timesteps i and $i+1$; and (3) optical relative measurements $\boldsymbol{z}_{\text{opt}} = {}^{C}_{T}\mathbf{T}$ between the target and chaser, expressed in the chaser's frame. Although not directly associated with a physical sensor, we additionally leverage dynamic motion models to constrain adjacent target states: an SE(2) and an SE(3) motion model for both the long and terminal phases, respectively, derived from sound hydrodynamic assumptions that can be made for a typical underwater docking scenario to an active target. Just as actual sensor measurements, these motion model predictions are also associated with their own factors in the graph.

Following the framework detailed in [10], we model the state estimation problem that arises from the previous description as a single factor graph optimization problem [23]. The factor graph corresponding to the scenario described beforehand is shown in Figure 2. Most of the factor nodes $\phi_{(\cdot)}$ in the graph encode constraints between their adjacent variable nodes, which are effectively the set of measurements and motion predictions $\mathbf{Z}$, except those that lie between the $\boldsymbol{x}_{\text{T}}$ and $\boldsymbol{x}_{\text{TT}}$ variable nodes. These factors enable the seamless change of representation of the target's state between $\mathbb{R}^3$ and SE(3)—a necessary step to avoid degeneracies or ill-constrained degrees of freedom during optimization. In other words, we want to consistently represent the belief that the system can have over the target: fully observable when in the terminal phase; partially observable when too far away. As variables of interest, we have the necessary state chains for the target and the chaser, and we additionally introduced two more node chains to estimate the target's dynamics when represented in $\mathbb{R}^3$ and in SE(3): we encode the constant target's heading and velocity in ${}^{W}\theta \in S^1$ and ${}^{T}v = ||{}^{T}\boldsymbol{v}|| \in \mathbb{R}$, respectively, which allow us to reason about the motion of the target and effectively render the state of the target as a pose in SE(2); and we track the target's 3D linear ${}^{T}\boldsymbol{v} \in \mathbb{R}^3$ and angular ${}^{T}\boldsymbol{\omega} \in \mathbb{R}^3$ velocities during the terminal phase.

The specific estimation problem we are trying to solve is the relative state estimation of both the chaser and the target. This can be posed as a SLAM problem, where we aim to solve, incrementally and in real-time, the maximum-a-posteriori (MAP) estimate

$$\boldsymbol{\Theta}^* = \arg\max_{\boldsymbol{\Theta}} p(\boldsymbol{\Theta}|\mathbf{Z}), \tag{1}$$

where

$$\boldsymbol{\Theta} = \{\mathbf{X}_C, \mathbf{X}_T, \mathbf{D}_T\} \tag{2}$$

contains the entire history of chaser states $\mathbf{X}_C = \{\boldsymbol{x}_{\mathrm{C}i}\}_{i=0:t_f}$ and target states $\mathbf{X}_T = \{\boldsymbol{x}_{\mathrm{T}i}, \boldsymbol{x}_{\mathrm{TT}i}\}_{i=0:t_f}$ (as a 3D landmark $\boldsymbol{x}_{\mathrm{T}}$ or a 3D pose $\boldsymbol{x}_{\mathrm{TT}}$), and t_f denotes the most recent timestep; and the history of all the target's motion model variables $\mathbf{D}_T = \{\boldsymbol{\omega}_d, \boldsymbol{v}_d, \theta_d, v_d\}_{d=0:d_f}$, where the subscript d_f represents the current dynamic's timestep that increases every time there is a change of representation of the target's state. The joint probability distribution $p(\boldsymbol{\Theta}|\mathbf{Z})$ is represented by our factor graph and $\mathbf{Z}$ represents the set of all hitherto collected measurements.

Now that we have laid out all of the preliminary information required to set the scene, we dive deep into the inner workings of our method.

IV. Methods

Our main focus herein is on the transition between phases (where we need to transition between fully observable and partially observable target representations depending on the available sensor information). We will start by briefly defining the chaser odometry and the long distance-only factors for which we mostly leverage the work from [10]. We continue with the description of the boundary factors that smoothly change the representation of the target's state, and finish with the definition of the terminal phase factors.

A. Chaser odometry factor

The recipe to generate a factor requires the definition of a few elements: an observation model, a residual, and a noise model. The chaser odometry factor ϕ_{odom}, which sits between consecutive chaser poses $\boldsymbol{x}_{\mathrm{C}i}$ and $\boldsymbol{x}_{\mathrm{C}j}$, uses an observation model $\boldsymbol{h}_{\text{odom}}(\boldsymbol{x}_{\mathrm{C}i}, \boldsymbol{x}_{\mathrm{C}j}) : \mathrm{SE}(3)\times\mathrm{SE}(3) \to \mathrm{SE}(3)$ to compute the relative transform ${}^{C_i}_{C_j}\mathbf{T}$ which is effectively the same as the measurement $\boldsymbol{z}_{\text{odom}}$ provided by the chaser's INS. With this information, it is straightforward to define the residual $\boldsymbol{\epsilon}_{\text{odom}}(\boldsymbol{x}_{\mathrm{C}i}, \boldsymbol{x}_{\mathrm{C}j}) : \mathrm{SE}(3) \times \mathrm{SE}(3) \to \mathbb{R}^6$ as

$$\epsilon_{\text{odom}} = \boldsymbol{h}_{\text{odom}}(\boldsymbol{x}_{\mathrm{C}i}, \boldsymbol{x}_{\mathrm{C}j}) \boxminus \boldsymbol{z}_{\text{odom}}, \tag{3}$$

where $\boxminus : \mathrm{SE}(3)\times\mathrm{SE}(3) \to \mathbb{R}^6$ is the on-manifold difference operator for $\mathrm{SE}(3)$ poses that results in a vector $\boldsymbol{\xi} \in \mathbb{R}^6$ that parameterizes the resulting *twist* on the tangent space with its origin at the identity at the frame C_j [24]. We finalize the definition of the factor by writing the full expression for ϕ_{odom}:

$$\phi_{\text{odom}}(\boldsymbol{x}_{\mathrm{C}i}, \boldsymbol{x}_{\mathrm{C}j}) \propto \exp\left\{-\frac{1}{2}\,||\boldsymbol{\epsilon}_{\text{odom}}(\boldsymbol{x}_{\mathrm{C}i}, \boldsymbol{x}_{\mathrm{C}j})||^2_{\boldsymbol{\Sigma}_{\text{odom}}}\right\}, \tag{4}$$

where $\boldsymbol{\Sigma}_{\text{odom}}$ is the covariance noise model for the chaser's odometry that is typically provided by the INS itself, and $||(\cdot)||^2_{\boldsymbol{\Sigma}} = (\cdot)^\top \boldsymbol{\Sigma}^{-1}(\cdot)$ denotes the Mahalanobis distance.

B. Long distance phase factors

For the long distance phase, we use the same factors as described in [10]. These consist of: (1) a relative (chaser to target) range and bearing factor ϕ_{rb}, whose measurement $\boldsymbol{z}_{rb}$ is provided by the USBL positioning system onboard the chaser; and (2), a motion model factor ϕ_{mm} that uses the constant velocity, heading, and depth, assumptions on the target dynamics to propagate its motion between consecutive positions. In [10], we found that even with these restraining assumptions our method can consistently handle adversarial target trajectories with a slowly varying heading and velocity.

For brevity, we will head straight to the definition of the factors and refer the reader to [10] for an in-depth description of the factor's content. The range and bearing factor ϕ_{rb} takes the form

$$\phi_{\text{rb}}(\boldsymbol{x}_{\mathrm{C}i}, \boldsymbol{x}_{\mathrm{T}i}) \propto \exp\left\{-\frac{1}{2}\left|\left|\begin{bmatrix}\epsilon_{\text{r}}(\boldsymbol{x}_{\mathrm{C}i}, \boldsymbol{x}_{\mathrm{T}i})\\ \boldsymbol{\epsilon}_{\text{b}}(\boldsymbol{x}_{\mathrm{C}i}, \boldsymbol{x}_{\mathrm{T}i})\end{bmatrix}\right|\right|^2_{\boldsymbol{\Sigma}_{\text{rb}}}\right\}, \tag{5}$$

where ϵ_{r} defines an error between the expected $||{}^C\boldsymbol{t}_{T/C}||$ and measured $\boldsymbol{z}_r$ relative range, $\boldsymbol{\epsilon}_{\text{b}}$ computes an on-manifold error between the expected ${}^C\hat{\boldsymbol{u}}_{T/C}$ and measured $\boldsymbol{z}_b$ 3D unit vector, and $\boldsymbol{\Sigma}_{\text{rb}}$ is the range-dependent noise model for the USBL measurements.

Next up, our $\mathrm{SE}(2)$ motion model factor ϕ_{mm} is given by

$$\begin{aligned}\phi_{\text{mm}}&(\boldsymbol{x}_{\mathrm{T}i}, \boldsymbol{x}_{\mathrm{T}j}, {}^Tv_d, {}^W\theta_d)\\ &\propto \exp\left\{-\frac{1}{2}\left|\left|\boldsymbol{\epsilon}_{\text{mm}}(\boldsymbol{x}_{\mathrm{T}i}, \boldsymbol{x}_{\mathrm{T}j}, {}^Tv_d, {}^W\theta_d)\right|\right|^2_{\boldsymbol{\Sigma}_{\text{mm}}}\right\},\end{aligned} \tag{6}$$

whose residual $\boldsymbol{\epsilon}_{\text{mm}}$ calculates the difference between $\boldsymbol{x}_{\mathrm{T}j}$ and the expected position $\hat{\boldsymbol{x}}_{\mathrm{T}j}$ computed via a simple kinematic model for a pose on $\mathrm{SE}(2)$, while $\boldsymbol{\Sigma}_{\text{mm}}$ denotes the associated uncertainty on the expected position.

C. Phase transition factors

Here is where our main contribution lies. Due to the need for a change of representation, we use a set boundary factors that seamlessly either expand $\mathbb{R}^3 \to \mathrm{SE}(3)$ or reduce $\mathrm{SE}(3) \to \mathbb{R}^3$ the state of the target, depending on the available sensor data—effectively transitioning the problem between the long distance and the terminal phase. The state expansion factor is a natural upgrade to the chaser's estimation system. However, we add the state reduction factor to the set of tools in our belt based on the assumption that the chaser can potentially lose visual tracking of the light fiducials from the target, leaving only the USBL relative position measurement to constrain the 6-DoF pose of the target—potentially resulting in an under-constrained optimization problem that can lead to deteriorating estimates [25].

Let us begin with the boundary expanding factor. Leading from the long distance/acoustic-only phase where the chaser has been solely constraining the position of the target $\boldsymbol{x}_{\mathrm{T}}$ with a range-bearing (USBL) measurement $\boldsymbol{z}_{rb}$, the chaser finally

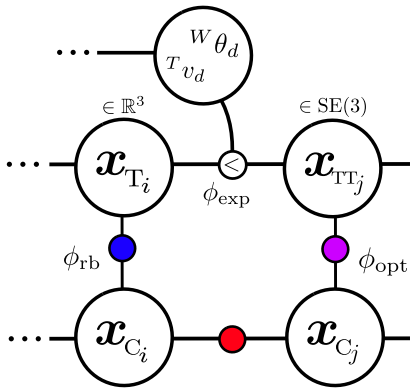

Fig. 3. Subgraph representing the expansion factor's neighborhood.

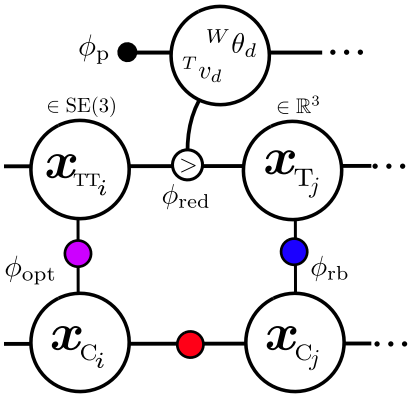

Fig. 4. Subgraph representing the reduction factor's neighborhood.

arrives at a close vicinity to its target. After positioning itself at a proper angle, it uses its onboard camera to compute high-accuracy and high-rate relative pose measurements $\boldsymbol{z}_{\mathrm{opt}} \in \mathrm{SE}(3)$ that resolve the full 6-DoF pose of the dynamic target $\boldsymbol{x}_{\mathrm{TT}}$. The specific subgraph on our factor graph where this scenario is modeled is shown in Figure 3. At this point, it is natural to want to change the representation of the target from $\mathbb{R}^3$ to $\mathrm{SE}(3)$, which leads us to the state expansion boundary factor ϕ_{exp}. This factor uses a simple prediction model

$$\boldsymbol{h}_{\mathrm{exp}}({}^{T}v_d) : \mathbb{R} \times \mathbb{R} \to \mathrm{SE}(3), \tag{7}$$

which computes a relative transformation between consecutive target frames T_i and T_j as

$$\boldsymbol{h}_{\mathrm{exp}}({}^{T}v_d) = \begin{bmatrix} {}^{T_i}_{T_j}\mathbf{R} & \boldsymbol{t}({}^{T}v_d \Delta t) \\ \mathbf{0}^{\top} & 1 \end{bmatrix} = {}^{T_i}_{T_j}\hat{\boldsymbol{T}}, \tag{8}$$

where ${}^{T_i}_{T_j}\mathbf{R} = \boldsymbol{I}_{3x3}$ since we are assuming constant heading for the target, and $\boldsymbol{t}({}^{T}v_d, \Delta t) = [{}^{T}v_d \Delta t,\ 0,\ 0]^{\top} = {}^{T_i}\boldsymbol{t}_{T_j/T_i}$ is the position change of the target in the direction of travel between the consecutive frames, expressed in the prior frame T_i. Δt is the time elapsed between timestep i and j. This motion model is used to define the factor's residual

$$\boldsymbol{\epsilon}_{\mathrm{exp}}(\boldsymbol{x}_{\mathrm{T}i}, \boldsymbol{x}_{\mathrm{TT}j}, {}^{T}v_d, {}^{W}\theta_d) : \mathbb{R}^3 \times \mathrm{SE}(3) \times \mathbb{R} \times S^1 \to \mathbb{R}^6, \tag{9}$$

which takes the form

$$\begin{aligned} \boldsymbol{\epsilon}_{\mathrm{exp}} &= \boldsymbol{h}_{\mathrm{exp}}({}^{T}v_d) \boxminus \left({}^{W}_{T_i}\mathbf{T}(\boldsymbol{x}_{\mathrm{T}i}, {}^{W}\theta_d) \ominus {}^{W}_{T_j}\mathbf{T} \right) \\ &= \boldsymbol{h}_{\mathrm{exp}}({}^{T}v_d) \boxminus {}^{T_i}_{T_j}\mathbf{T}, \end{aligned} \tag{10}$$

where $\ominus : \mathrm{SE}(3) \times \mathrm{SE}(3) \to \mathrm{SE}(3)$ denotes the inverse composition between two poses in homogeneous coordinates, ${}^{W}_{T_j}\mathbf{T} = \boldsymbol{x}_{\mathrm{TT}j}$, and

$${}^{W}_{T_i}\mathbf{T}(\boldsymbol{x}_{\mathrm{T}i}, {}^{W}\theta_d) = \begin{bmatrix} \mathbf{R}({}^{W}\theta_d) & \boldsymbol{x}_{\mathrm{T}i} \\ \mathbf{0}^{\top} & 1 \end{bmatrix} \tag{11}$$

is the pose of the target at T_i computed using the most recent position $\boldsymbol{x}_{\mathrm{T}i}$ and heading ${}^{W}\theta_d$. This finally culminates in the definition of the state expansion factor, which takes the form:

$$\begin{aligned} &\phi_{\mathrm{exp}}(\boldsymbol{x}_{\mathrm{T}i}, \boldsymbol{x}_{\mathrm{TT}j}, {}^{T}v_d, {}^{W}\theta_d) \\ &\quad \propto \exp\left\{ -\frac{1}{2} \left|\left| \boldsymbol{\epsilon}_{\mathrm{exp}}(\boldsymbol{x}_{\mathrm{T}i}, \boldsymbol{x}_{\mathrm{TT}j}, {}^{T}v_d, {}^{W}\theta_d) \right|\right|^2_{\boldsymbol{\Sigma}_{\mathrm{exp}}} \right\}, \end{aligned} \tag{12}$$

with $\boldsymbol{\Sigma}_{\mathrm{exp}}$ as the noise model for the expansion factor.

The state reduction boundary factor ϕ_{red} is an important robustness measure that avoids underconstraining the orientation of the target during optimization, in the case of the chaser driving astray from the target to the point that the light beacons are no longer visible and no optical feedback is possible. The corresponding subgraph for this scenario is shown in Figure 4.

In contrast to the state expansion factor, the prior state involved in this factor is the target's pose $\boldsymbol{x}_{\mathrm{TT}j} \in \mathrm{SE}(3)$, while the subsequent state $\boldsymbol{x}_{\mathrm{T}j} \in \mathbb{R}^3$ is back to being only the 3D position of the target. Notice that now, since we no longer have high-rate optical measurements, we re-establish the motion model between factor ϕ_{mm} in (6) with a new set of motion variables $({}^{T}v_{d+1}, {}^{W}\theta_{d+1})$, which are initialized with a freshly computed prior factor $\phi_{\mathrm{p}}({}^{T}v_{d+1}, {}^{W}\theta_{d+1})$. This factor uses as mean value and prior noise for the velocity the most recent estimate of the 3D velocity $||\,{}^{T}\boldsymbol{v}_d|| = {}^{T}v_{d+1} = \mathcal{N}(||\,{}^{T}\boldsymbol{v}_d||, \sigma^2_{\boldsymbol{v}})$, while the heading is computed from the latest target pose through a function $\theta(\boldsymbol{x}_{\mathrm{TT}i}) : \mathrm{SE}(3) \to S^1$ that simply extracts the heading angle ${}^{W}\theta_{d+1}$ from $\boldsymbol{x}_{\mathrm{TT}i}$.

The state reduction factor uses the same prediction model $\boldsymbol{h}_{\mathrm{red}}$ used for the $\mathrm{SE}(2)$ motion model factor (6), with the exception that the position $\boldsymbol{x}_{\mathrm{T}i}$ in this case is computed by a an observation model $\boldsymbol{t}(\boldsymbol{x}_{\mathrm{TT}i}) : \mathrm{SE}(3) \to \mathbb{R}^3$, where $\boldsymbol{t}(\boldsymbol{x}_{\mathrm{TT}i}) = {}^{W}\boldsymbol{t}_{T_i/W}$, which only accesses the translation vector in $\boldsymbol{x}_{\mathrm{TT}i}$—defining it as the mapping $\boldsymbol{h}_{\mathrm{red}} : \mathrm{SE}(3) \times \mathbb{R} \times S^1 \to \mathbb{R}^3$. The full expression for the prediction model, takes the form:

$$\begin{aligned} &\boldsymbol{h}_{\mathrm{red}}(\boldsymbol{x}_{\mathrm{TT}i}, {}^{T}v_{d+1}, {}^{W}\theta_{d+1}) \\ &\quad = \boldsymbol{R}({}^{W}\theta_{d+1})\boldsymbol{t}(\boldsymbol{x}_{\mathrm{TT}i}) + \boldsymbol{t}({}^{T}v_{d+1}, \Delta t) = \hat{\boldsymbol{x}}_{\mathrm{T}j}. \end{aligned} \tag{13}$$

where $\boldsymbol{R}({}^{W}\theta_{d+1}) \in SO(3)$ is the rotation matrix associated with the heading angle ${}^{W}\theta_{d+1}$, and $\boldsymbol{t}({}^{T}v_{d+1}) \in \mathbb{R}^3$ is the translation due to the target's velocity in the time Δt.

The residual

$$\boldsymbol{\epsilon}_{\text{red}}(\boldsymbol{x}_{\text{TT}i}, \boldsymbol{x}_{\text{T}j}, {}^{T}v_{d+1}, {}^{W}\theta_{d+1}) : \text{SE}(3)\times\mathbb{R}^3\times\mathbb{R}\times S^1 \rightarrow \mathbb{R}^3, \tag{14}$$

defines an error on the adjacent 3D position of the target $\boldsymbol{x}_{\text{T}j}$ as

$$\boldsymbol{\epsilon}_{\text{red}} = h_{\text{red}}(\boldsymbol{x}_{\text{TT}i}, {}^{T}v_{d+1}, {}^{W}\theta_{d+1}) - \boldsymbol{x}_{\text{T}j}, \tag{15}$$

which is finally used to compute the sought-after state reduction factor

$$\phi_{\text{red}}(\boldsymbol{x}_{\text{TT}i}, \boldsymbol{x}_{\text{T}j}, {}^{T}v_{d+1}, {}^{W}\theta_{d+1}) \propto \exp\left\{-\frac{1}{2}\left|\left|\boldsymbol{\epsilon}_{\text{red}}(\boldsymbol{x}_{\text{TT}i}, \boldsymbol{x}_{\text{T}j}, {}^{T}v_{d+1}, {}^{W}\theta_{d+1})\right|\right|^2_{\boldsymbol{\Sigma}_{\text{red}}}\right\}, \tag{16}$$

with $\boldsymbol{\Sigma}_{\text{red}}$ being the factor's noise model.

Now that we have detailed the boundary factors, the next section sheds light on the factor that is computed using optical feedback during the terminal approach phase.

D. Terminal phase factors and representation

Typically, for underwater docking applications, the terminal homing phase will require higher navigation accuracy and a faster feedback rate than the commonly provided by acoustic measurements, to ensure the successful final approach of the chaser to its target. This notable jump in accuracy and sampling requirements can be easily fulfilled using an optical feedback system. During the terminal phase (center section of the factor graph in Figure 2), we use relative pose measurements from a monocular camera on the chaser to the center of the light beacon arrangement on the target. It is worthy to note, that there exists a fixed and known extrinsic calibration between the light fiducials and the target's frame of reference, which for clarity reasons is being omitted in the pictorial description of the graph. The front-end image processing and pose estimation approach we use to compute such measurements is thoroughly detailed in [26]. This front-end computes a relative pose $\boldsymbol{z}_{\text{opt}} = {}^{C_i}_{T_i}\mathbf{T}$ that is used to compute a factor $\phi_{\text{opt}} : \text{SE}(3)\times\text{SE}(3) \rightarrow \mathbb{R}^6$, which is effectively the same as (4). We write the expression for the optical factor as

$$\phi_{\text{opt}}(\boldsymbol{x}_{\text{C}i}, \boldsymbol{x}_{\text{TT}i}) \propto \exp\left\{-\frac{1}{2}\left|\left|\boldsymbol{\epsilon}_{\text{opt}}(\boldsymbol{x}_{\text{C}i}, \boldsymbol{x}_{\text{TT}i})\right|\right|^2_{\boldsymbol{\Sigma}_{\text{opt}}}\right\}, \tag{17}$$

where $\boldsymbol{\Sigma}_{\text{opt}}$ is the measurement $\boldsymbol{z}_{\text{opt}}$ noise model computed by the front-end pose estimation module, and the residual

$$\boldsymbol{\epsilon}_{\text{opt}} = \boldsymbol{h}_{\text{opt}}(\boldsymbol{x}_{\text{C}i}, \boldsymbol{x}_{\text{TT}i}) \boxminus \boldsymbol{z}_{\text{opt}} = {}^{C_i}_{T_i}\hat{\boldsymbol{T}} \boxminus \boldsymbol{z}_{\text{opt}}. \tag{18}$$

Important to note that this optical constraint is a parallel constraint to the USBL one and further strongly correlates our two main pose chains in the factor graph.

Once we have changed the representation of the target to SE(3), it is then possible for us to start tracking the linear ${}^{T}\boldsymbol{v}$ and angular ${}^{T}\boldsymbol{\omega}$ velocities of the target (as shown in Figure 2). Apart from smoothing the resulting estimates by means of a 3D motion model, knowing the velocities of the target can help inform the consecutive tasks further down the docking pipeline, e.g. motion planning and control. We initialize the velocity variable nodes with a prior factor $\phi_{\text{p}}({}^{T}\boldsymbol{v}_i, {}^{T}\boldsymbol{\omega}_i)$, whose values are calculated as

$$\begin{aligned} {}^{T}\boldsymbol{v}_i &= \boldsymbol{\mathcal{N}}([{}^{T}v_d, 0, 0]^\top, \boldsymbol{\Sigma}_v), \\ {}^{T}\boldsymbol{\omega}_i &= \boldsymbol{\mathcal{N}}(\mathbf{0}, \boldsymbol{\Sigma}_w), \end{aligned} \tag{19}$$

where $\boldsymbol{\Sigma}_v = \text{diag}(\sigma_v^2)$ is a diagonal covariance matrix with the most current noise estimate of the target's velocity, and $\boldsymbol{\Sigma}_w$ is set accordingly. The target odometry factor ϕ_{to} is based on the error on the relative transformation ${}^{T_i}_{T_j}\mathbf{T}$ calculated by time-integrating the twist of the target at T_i:

$$\begin{aligned} \boldsymbol{h}_{to}({}^{T}\boldsymbol{v}_i, {}^{T}\boldsymbol{\omega}_i, \Delta t) &: \mathbb{R}^3\times\mathbb{R}^3 \rightarrow \mathbb{R}^6 \\ \boldsymbol{h}_{to} &= \begin{bmatrix} {}^{T}\boldsymbol{\omega}_i \\ {}^{T}\boldsymbol{v}_i \end{bmatrix}\Delta t = {}^{T_i}_{T_j}\hat{\boldsymbol{\xi}}, \end{aligned} \tag{20}$$

where

$$\text{Exp}\left({}^{T_i}_{T_j}\hat{\boldsymbol{\xi}}\right) = {}^{T_i}_{T_j}\hat{\boldsymbol{T}}. \tag{21}$$

$\text{Exp}(\cdot) : \mathbb{R}^6 \rightarrow \text{SE}(3)$ is the exponential map that defines a retraction from the tangent space back to the SE(3) manifold [24]. To define the residual we use the following expressions:

$$\begin{aligned} &\boldsymbol{\epsilon}_{\text{to}}(\boldsymbol{x}_{\text{TT}i}, \boldsymbol{x}_{\text{TT}j}, {}^{T}\boldsymbol{v}_i, {}^{T}\boldsymbol{\omega}_i) : \text{SE}(3)\times\text{SE}(3)\times\mathbb{R}^3\times\mathbb{R}^3 \rightarrow \mathbb{R}^6 \\ &\boldsymbol{\epsilon}_{\text{to}} = \boldsymbol{h}_{\text{to}}({}^{T}\boldsymbol{v}_i, {}^{T}\boldsymbol{\omega}_i, \Delta t) \boxminus \left({}^{W}_{T_i}\mathbf{T} \ominus {}^{W}_{T_j}\mathbf{T}\right) \\ &\quad = \boldsymbol{h}_{\text{exp}}({}^{T}v, \Delta t) \boxminus {}^{T_i}_{T_j}\mathbf{T}. \end{aligned} \tag{22}$$

We write down the complete expression for the target 3D odometry factor as

$$\phi_{\text{to}}(\boldsymbol{x}_{\text{TT}i}, \boldsymbol{x}_{\text{TT}j}, {}^{T}\boldsymbol{v}_i, {}^{T}\boldsymbol{\omega}_i) \propto \exp\left\{-\frac{1}{2}\left|\left|\boldsymbol{\epsilon}_{\text{to}}(\boldsymbol{x}_{\text{TT}i}, \boldsymbol{x}_{\text{TT}j}, {}^{T}\boldsymbol{v}_i, {}^{T}\boldsymbol{\omega}_i)\right|\right|^2_{\boldsymbol{\Sigma}_{\text{to}}}\right\}, \tag{23}$$

where $\boldsymbol{\Sigma}_{\text{to}}$ is the noise model associated to the computed odometry.

Last, it is important to highlight that even after the change of representation, and after crossing the boundary into the terminal phase, we still use the information provided by the USBL and include it in the factor graph. This range-bearing factor $\phi_{\text{rb}}(\boldsymbol{x}_{\text{C}i}, \boldsymbol{x}_{\text{TT}i})$, although associated to the target's pose $\boldsymbol{x}_{\text{TT}i}$ instead of to its position $\boldsymbol{x}_{\text{T}}$, remains virtually the same as detailed in (5).

V. Simulation Results

To verify the performance of our state estimation method, we upgraded the simulated environment used in [10] using the Stonefish simulator [27], to include the light fiducials on the target AUV and a monocular camera on the chaser AUV. We use the Robot Operating System (ROS) as the middleware in our software stack and leverage its compatibility with the Stonefish simulator to record the dataset with the sensor information needed for the evaluation of our method. The factor graph SLAM back-end system is all developed using the Georgia Tech Smoothing and Mapping (GTSAM [28]) library for C++, whose modularity allows to routinely develop the factors required by our solution. We use the iSAM2 [29] solver implementation available in the GTSAM to compute real-time estimates that we use

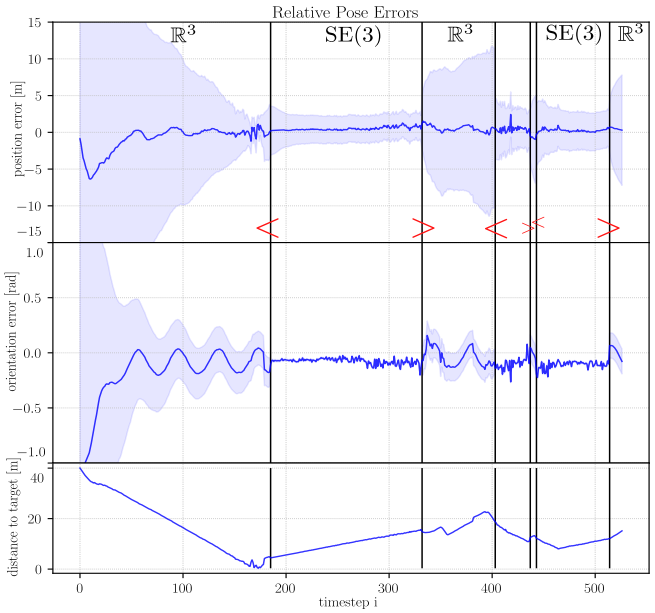

Fig. 5. Plot showing the relative pose errors between the real-time estimate and the ground truth from the simulator. The vertical lines denote the boundary between a change of representation of the target's state from $\mathbb{R}^3$ to SE(3) (denoted by $<$) and from SE(3) to $\mathbb{R}^3$ ($>$).

to quantify the performance of our approach. By real-time estimates, we refer to the latest estimate $\boldsymbol{x}^*_{t_i|0:t_i}$ and not the fully smoothed solution $\boldsymbol{x}^*_{t_i|0:t_f}$ where $t_i \in [t_0, ..., t_f]$.

The simulated experiment consisted in the target traveling with constant heading and velocity. The chaser, starting far behind the target, travels in the same direction using a simple heading controller (agnostic of the target's state), until eventually catching up with the target. Once the optical front-end started estimating the relative poses, the velocity of the chaser was manipulated manually to keep the target in sight. Figure 5 (bottom) shows the ground truth distance-to-target, further clarifying the scenario.

The processed results are shown in Figure 5. The top plots show the error of the estimated relative pose between the chaser and the target ${}^C_T\mathbf{T}$, as compared to the ground truth values from the simulator. The two top plots show the position and orientation errors, respectively, while the bottom plot details the ground truth distance to target to give the reader more perspective about the scenario conditions during each timestep. The vertical lines on the plots determine the boundary between a change on the target's representation SE(3) $\rightarrow \mathbb{R}^3$ or $\mathbb{R}^3 \rightarrow$ SE(3).

As expected, we can see a drop in the error and its associated uncertainty whenever there is a target's state expansion ($\mathbb{R}^3 \rightarrow$ SE(3)), brought by the acquisition of the optical pose constraints $\boldsymbol{z}_{opt}$. The opposite occurs at the reduction boundary, where the errors and uncertainties show an important increase—which is consistent with the noisy nature of the USBL measurements and the sudden loss of information regarding the roll and pitch of the target. This are the sought-after behaviors we want our system to showcase: (i) to be able to seamlessly transfer information between boundaries/phases, i.e., to not have the mean of the estimate abruptly jump back and forth when transitioning between phases; and (ii) to achieve (i) while expressing the true belief we have in the target's state, which essentially means that we want our state estimation system to consistently represent the uncertainty associated to having a partially- or fully-observable target's state. (i) can easily be appreciated by tracking the solid line in the error plots: the slight jump on the orientation error plot (along with the oscillating error) while in the long-distance phase in $\mathbb{R}^3$ is due to the fact the the target is not actually following a straight line but a sinusoidal one in the simulator—due to the limits of the depth controller. (ii) is also straightforward to see when noticing that the position and orientation uncertainties are fully associated to the range-dependent USBL noise model during the long distance phase $\mathbb{R}^3$, and to the high-accuracy optical measurements during the terminal phase SE(3).

Additional to the seamless transition between phases, we can observe how the optical measurements and the target's SE(3) motion model work together to achieve relatively low (to those provided by the USBL) error regime, a generally desired performance trait required for several proximity operation scenarios—the chaser has to be certain enough of the state of the target when, e.g., hard-docking.

VI. Conclusions and Future Work

We conclude the present work with a two-fold contribution towards the field of state estimation for autonomous underwater docking with dynamic targets. First, we detailed and showcased a single factor graph SLAM approach for estimating the relative state between the chaser and the target throughout the two main navigation phases of an underwater proximity operation. Second, we presented and showcased the use of state expansion and reduction boundary factors that allow the back-and-forth seamless transitioning between the long distance underwater docking phase, where the target's state is only partially observable (point landmark on $\mathbb{R}^3$), and the terminal phase where we can fully observe the pose of the target (on SE(3)).

As future work, we will provide further insights on the inner workings of the present methods by benchmarking its performance on real world datasets, as well as detailing the practicalities involved on its integration on a real AUV platform. Furthermore, we will look at relaxing the constraints on the target's motion during the long distance phase, by studying different approaches for dealing with unknown target dynamics.

References

[1] J. Bellingham, K. Streitlien, J. Overland, S. Rajah, P. Stein, J. Stannard, W. Kirkwood, and D. Yoerger, "An Arctic Basin Observational Capability Using AUVs," *Oceanography*, vol. 13, no. 2, pp. 64–70, 2000.

[2] H. Singh, J. Catipovic, R. Eastwood, L. Freitag, H. Henriksen, F. Hover, D. Yoerger, J. Bellingham, and B. Moran, "An integrated approach to multiple AUV communications, navigation and docking," in *OCEANS 96 MTS/IEEE Conference Proceedings. The Coastal Ocean - Prospects for the 21st Century*, vol. 1, pp. 59–64 vol.1, Sept. 1996.

[3] B. R. Page, R. Lambert, J. Chavez-Galaviz, and N. Mahmoudian, "Underwater Docking Approach and Homing to Enable Persistent Operation," *Frontiers in Robotics and AI*, vol. 8, 2021.

[4] P. Ridao, M. Carreras, D. Ribas, P. J. Sanz, and G. Oliver, "Intervention AUVs: The next challenge," *Annual Reviews in Control*, vol. 40, pp. 227–241, Jan. 2015.

[5] T. Palmer, D. Ribas, P. Ridao, and A. Mallios, "Vision based localization system for AUV docking on subsea intervention panels," in *OCEANS 2009-EUROPE*, pp. 1–10, May 2009.

[6] E. I. Sarda and M. R. Dhanak, "Launch and Recovery of an Autonomous Underwater Vehicle From a Station-Keeping Unmanned Surface Vehicle," *IEEE Journal of Oceanic Engineering*, vol. 44, pp. 290–299, Apr. 2019. Conference Name: IEEE Journal of Oceanic Engineering.

[7] Z. Zhou, Y. Jiang, Y. Li, C. Jian, and Y. Sun, "A single acoustic beacon-based positioning method for underwater mobile recovery of an AUV," *International Journal of Advanced Robotic Systems*, vol. 15, p. 172988141880173, Sept. 2018.

[8] Hydroid, "Underwater mobile docking of autonomous underwater vehicles," in *2012 Oceans*, pp. 1–15, Oct. 2012. ISSN: 0197-7385.

[9] R. S. McEwen, B. W. Hobson, L. McBride, and J. G. Bellingham, "Docking Control System for a 54-cm-Diameter (21-in) AUV," *IEEE Journal of Oceanic Engineering*, vol. 33, pp. 550–562, Oct. 2008. Conference Name: IEEE Journal of Oceanic Engineering.

[10] A. Teran Espinoza, A. Teran Espinoza, J. Folkesson, N. Rolleberg, P. Sigray, and J. Kuttenkeuler, "Simultaneous trajectory estimation and mapping for autonomous underwater proximity operations," *arXiv preprint arXiv:2309.08780*, 2023.

[11] A. Terán Espinoza, H. Hettrick, K. Albee, A. Cabrales Hernandez, and R. Linares, "End-to-end framework for close proximity in-space robotic missions," in *70th International Astronautical Congress (IAC)*, (Washington, DC, USA), International Astronautical Federation, Oct. 2019.

[12] M. Feezor, F. Yates Sorrell, P. Blankinship, and J. Bellingham, "Autonomous underwater vehicle homing/docking via electromagnetic guidance," *IEEE Journal of Oceanic Engineering*, vol. 26, pp. 515–521, Oct. 2001. Conference Name: IEEE Journal of Oceanic Engineering.

[13] M. Lin, R. Lin, C. Yang, D. Li, Z. Zhang, Y. Zhao, and W. Ding, "Docking to an underwater suspended charging station: Systematic design and experimental tests," *Ocean Engineering*, vol. 249, p. 110766, Apr. 2022.

[14] L. Zhang, Y. Li, G. Pan, Y. Zhang, and S. Li, "Terminal Stage Guidance Method for Underwater Moving Rendezvous and Docking Based on Monocular Vision," in *OCEANS 2019 - Marseille*, pp. 1–6, June 2019.

[15] L. Brignone, M. Perrier, and C. Viala, "A fully autonomous docking strategy for Intervention AUVs," in *OCEANS 2007 - Europe*, pp. 1–6, June 2007.

[16] N. Palomeras, P. Ridao, D. Ribas, and G. Vallicrosa, "Autonomous I-AUV Docking for Fixed-base Manipulation," *IFAC Proceedings Volumes*, vol. 47, pp. 12160–12165, Jan. 2014.

[17] M. F. Fallon, J. Folkesson, H. McClelland, and J. J. Leonard, "Relocating underwater features autonomously using sonar-based slam," *IEEE Journal of Oceanic Engineering*, vol. 38, no. 3, pp. 500–513, 2013.

[18] J. Vaganay, P. Baccou, and B. Jouvencel, "Homing by acoustic ranging to a single beacon," in *OCEANS 2000 MTS/IEEE Conference and Exhibition. Conference Proceedings (Cat. No.00CH37158)*, vol. 2, pp. 1457–1462 vol.2, Sept. 2000.

[19] L. Ruan, S. Chen, J. Zhou, D. Zeng, and Y. Xu, "A Factor Graph Method for AUV Navigation in the Mobile Docking Progress," in *Global Oceans 2020: Singapore – U.S. Gulf Coast*, pp. 1–5, Oct. 2020. ISSN: 0197-7385.

[20] Z. Yan, P. Gong, and W. Zhang, "Dynamic Docking Technology between AUV and Mobile Mothership," in *2020 Chinese Control And Decision Conference (CCDC)*, pp. 3045–3049, Aug. 2020. ISSN: 1948-9447.

[21] T. Ma, S. Chen, L. Ruan, and Y. Xu, "A vision-integrated navigation method in auv terminal mobile docking based on factor graph optimization," in *2023 8th International Conference on Automation, Control and Robotics Engineering (CACRE)*, pp. 383–388, 2023.

[22] G. D. Watt, A. R. Roy, J. Currie, C. B. Gillis, J. Giesbrecht, G. J. Heard, M. Birsan, M. L. Seto, J. A. Carretero, R. Dubay, and T. L. Jeans, "A Concept for Docking a UUV With a Slowly Moving Submarine Under Waves," *IEEE Journal of Oceanic Engineering*, vol. 41, pp. 471–498, Apr. 2016. Conference Name: IEEE Journal of Oceanic Engineering.

[23] F. Dellaert and M. Kaess, "Factor Graphs for Robot Perception," *Foundations and Trends® in Robotics*, vol. 6, pp. 1–139, Aug. 2017. Publisher: Now Publishers, Inc.

[24] J. Sola, J. Deray, and D. Atchuthan, "A micro lie theory for state estimation in robotics," *arXiv preprint arXiv:1812.01537*, 2018.

[25] A. Hinduja, B.-J. Ho, and M. Kaess, "Degeneracy-aware factors with applications to underwater slam," in *2019 IEEE/RSJ International Conference on Intelligent Robots and Systems (IROS)*, pp. 1293–1299, IEEE, 2019.

[26] J. Edlund, "Robust light source detection for auv docking," Master's thesis, KTH, School of Electrical Engineering and Computer Science (EECS), 2023.

[27] P. Cieślak, "Stonefish: An Advanced Open-Source Simulation Tool Designed for Marine Robotics, With a ROS Interface," in *OCEANS 2019 - Marseille*, pp. 1–6, June 2019.

[28] F. Dellaert and G. Contributors, "borglab/gtsam," May 2022.

[29] M. Kaess, H. Johannsson, R. Roberts, V. Ila, J. J. Leonard, and F. Dellaert, "isam2: Incremental smoothing and mapping using the bayes tree," *The International Journal of Robotics Research*, vol. 31, no. 2, pp. 216–235, 2012.